Combinatorial metamaterials with multiple degrees of freedom

Institute of Physics, University of Amsterdam

Aleksi Bossart
Advisor: Corentin Coulais

April 13, 2019

Abstract

We investigate a new class of multimodal mechanical metamaterials arising from tiling the plane with a single bimodal cell. We propose an alternative to the compatibility matrix description of the zero modes in the form of a vertex model based on the linearized geometric constraints. The associated R-matrix is a tensor of order 5 respecting the ice rule, which hints at integrability. Using this model, we describe the rich mechanism phenomenology of our material. In particular, we present multimodal metamaterials with a number of zero modes that remains constant with increasing system size, as well as peculiar linearly decaying modes. We validate our predictions using a combination of finite-element simulations and elasticity experiments.

Contents

Chapter 1

Tilings with a bimodal primitive cell

1.1 Motivation

1.2 Primitive cell geometry and index theorem

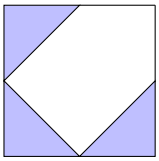

Figure 1.1: The bimodal unit cell.

Repeating this primitive cell with arbitrary orientations on a Lieb lattice yields a variety of configurations. Our main purpose is to describe and classify the rich spectrum of elastic behaviour of these configurations.

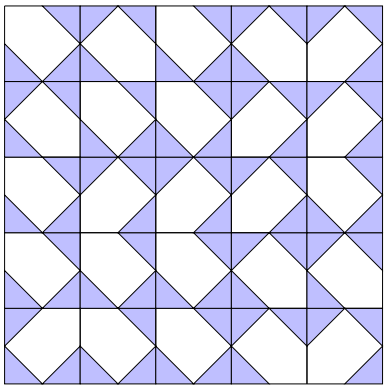

Figure 1.2: An arbitrary tiling with the bimodal unit cell.

The Maxwell index theorem [1] immediately provides us with a relation between the number of states of self-stress and the number of mechanisms,

$$dN - c = \frac{d(d+1)}{2} + N_M - N_{SS}, \tag{1.1}$$

which we can evaluate for our pentagon-paved Lieb lattices. Each cell has a contribution of $N = 3$

and $c = 7$, with an additional contribution of $N = 2(n + m) + 1$ and $c = 2(n + m)$ from the boundary. Constraining the displacements to a plane, this yields

$$N_M - N_{SS} = 2(3nm + 2(n + m) + 1) - (7nm + 2(n + m)) - 3 = 2(n + m) - nm - 1. \tag{1.2}$$

Chapter 2

An exotic vertex model

The bimodal nature of the above cell arises from purely geometrical considerations. To get a more quantitative theory, these geometric constraints can be encoded in three trigonometric equations. We then linearize these equations and represent the result graphically. This yields a nice design procedure, along with an exotic vertex model.

2.1 Linearization of the geometric constraints

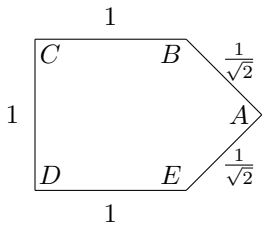

Figure 2.1: The prismatic pentagon in the reference position.

Following [2], the geometric constraints put forward by the side lengths of the pentagon can be expressed as[1]

$$A + B + C + D + E = 3\pi, \tag{2.1}$$

$$1 - \cos(A) = 3 - 2\cos(C) - 2\cos(D) + 2\cos(C + D), \tag{2.2}$$

$$\sin(D) - \frac{\sin(D + E)}{\sqrt{2}} = \sin(C) - \frac{\sin(C + B)}{\sqrt{2}}. \tag{2.3}$$

We can linearize these expressions around the

$$A = \frac{\pi}{2} + \alpha \quad B = \frac{3\pi}{4} + \beta \quad C = \frac{\pi}{2} + \gamma \quad D = \frac{\pi}{2} + \delta \quad E = \frac{3\pi}{4} + \epsilon \tag{2.4}$$

choice of angles, yielding the following system of linear equations,

[1]The complex number notation is much clearer, as usual.

$$\begin{pmatrix} 1 & 1 & 1 & 1 & 1 \\ 1 & -2 & & & -2 \\ & 1 & 1 & -1 & -1 \end{pmatrix} \begin{pmatrix} \alpha \\ \delta \\ \epsilon \\ \beta \\ \gamma \end{pmatrix} = \begin{pmatrix} 0 \\ 0 \\ 0 \end{pmatrix} \rightarrow \begin{pmatrix} \alpha \\ \delta \\ \epsilon \end{pmatrix} = \begin{pmatrix} -2 & -2 \\ -1 & -2 \\ 2 & 3 \end{pmatrix} \begin{pmatrix} \beta \\ \gamma \end{pmatrix}. \tag{2.5}$$

As expected from the index theorem, there are two free parameters. We express this constraint graphically in Fig.2.2, by drawing the two modes of our pentagon in a convenient basis. Any linear combination of those two vertices is thus also an acceptable vertex.

2.2 Formulation of the vertex model

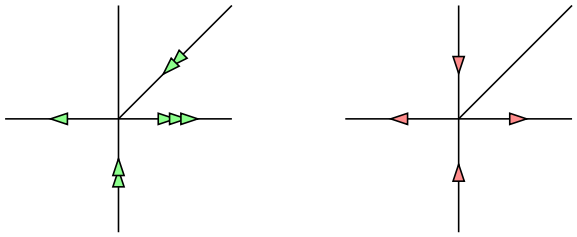

Figure 2.2: Graphical representation of the linearized geometric constraints.

Note that the red vertex in Fig.2.2 depicts a common finite mechanism[2].

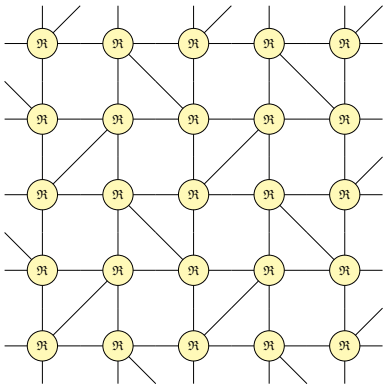

Figure 2.3: A network of contracted $\mathfrak{R}$-matrices.

The shape of the vertex indicates that the R-matrix should be a tensor of order 5. Futhermore, the linear combination freedom implies that the edge vector spaces are infinite. The ice rule is enforced (also in the full nonlinear theory) by the conserved sum of angles. A potentially successful formulation thus implies using an odd-dimensional multlinear operator as the R-matrix, with a kernel that respects our restricted ice rule in some way.

By an angle-fixing argument, the model can be trivially extended to 6, 7 and 8 edges per vertex. Indeed, we can take our existing vertex and add a diagonal edge in either of the three available corners. If we then fix the value of one of these diagonal edges, we reduce the problem to the pentagonal case. Since this yields three independent vertices, it exhausts the available modes.

[2]Set all the greek letter angles except χ in Eq.2.6 equal to zero and plug them in Eqs.2.1 to 2.3 to prove finiteness. Alternatively, squeeze the imaginary square in your head.

2.3 Vertex configurations of fundamental mechanisms

It is useful to describe the actuation of a few fundamental mechanisms in the vertex model framework, in order to understand the modes of the tilings described in the next chapter.

2.3.1 Local building blocks

We will first consider all the possible *contractions* of diagonal legs, since they give rise to the non-trivial modes. Considering the next-neighbour contraction of Fig.2.4, we see that any choice of arrows on the left-hand vertex must be mirrored (with reversed directions) on the right-hand vertex.

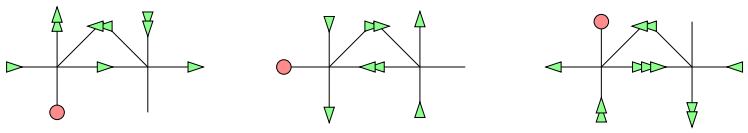

Figure 2.4: The three non-trivial vertex configurations of a next-neighbour contraction.

The next contraction possibility is a next-to-next-neighbour interaction, as depicted in Fig.2.5. There are more available configurations, since a simple contraction is less demanding than a double.

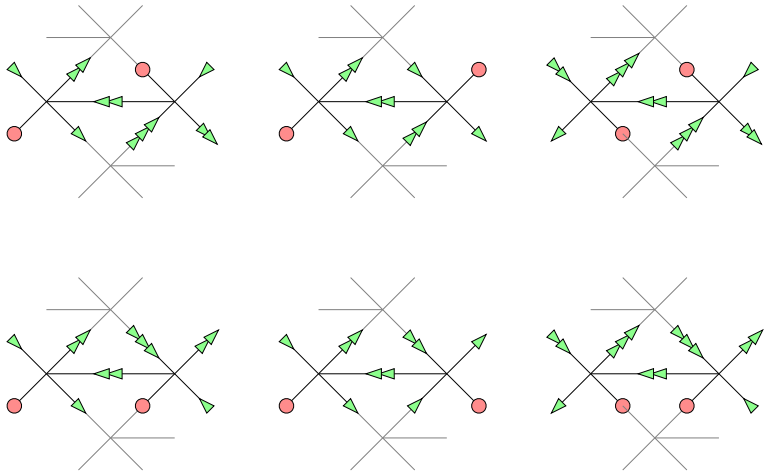

Figure 2.5: Next-to-next neighbour contractions with two interacting edges.

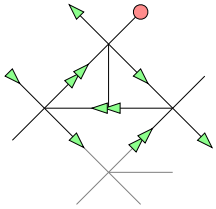

Figure 2.6: Next-to-next neighbour contractions with three interacting edges.

2.3.2 Global modes

Using the building blocks of Sec.2.3.1, we can describe a few global modes.

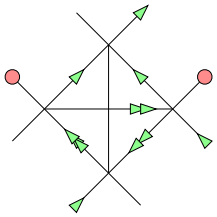

Figure 2.7: Next-to-next neighbour contractions with four interacting edges.

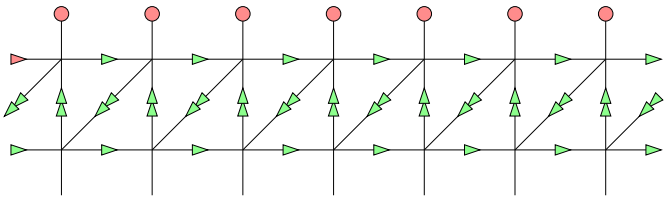

Figure 2.8: Vertex configuration of an activated bump mechanism. The red points/arrows denote fixed angles, while the green ones are constrained by the former.

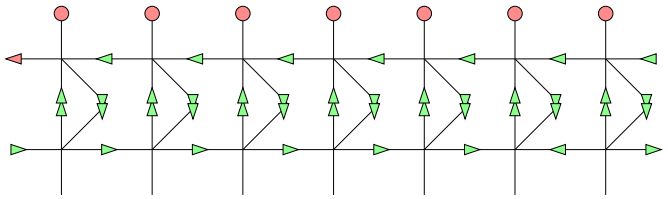

Figure 2.9: Vertex configuration of an activated antibump mechanism. The red points/arrows denote fixed angles, while the green ones are constrained by the former.

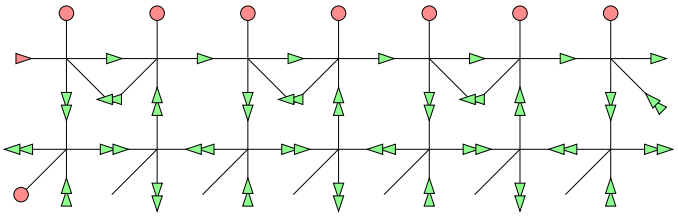

Figure 2.10: Vertex configuration of an activated "domain wall" mechanism. The red points denote fixed angles.

The shape of the identified fundamental mechanisms suggests that a transfer matrix formulation of the combinatorial problem might be accessible.

The linear decay mechanism depicted in Fig.2.11 is potentially dangerous, since the linear approximation underlying the vertex model breaks down after a certain length. To tackle this problem, we use the finite mechanism at our disposal and linearize around

$$A = \frac{\pi}{2} + \alpha \quad B = \frac{3\pi}{4} + \chi + \beta \quad C = \frac{\pi}{2} - \chi + \gamma \quad D = \frac{\pi}{2} + \chi + \delta \quad E = \frac{3\pi}{4} - \chi + \epsilon, \tag{2.6}$$

and obtain the modified system of equations

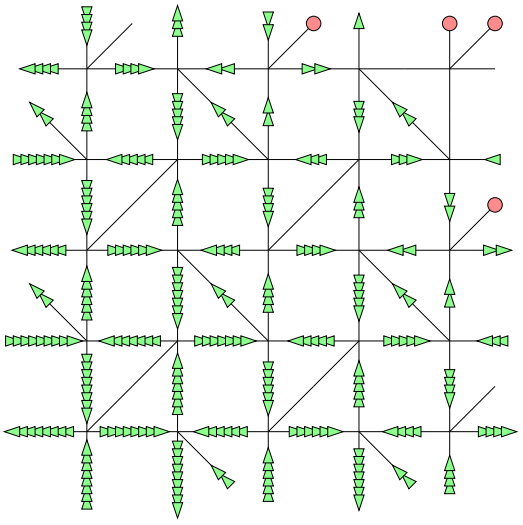

Figure 2.11: Vertex configuration of an activated linear decay mechanism. The red points/arrows denote fixed angles, while the green ones are constrained by the former.

$$\begin{pmatrix} 1 & 1 & 1 & 1 & 1 \\ 1 & -2c & & & -2c \\ & 1-2s & 1 & -1 & -1-2s \end{pmatrix} \begin{pmatrix} \alpha \\ \delta \\ \epsilon \\ \beta \\ \gamma \end{pmatrix} = \begin{pmatrix} 0 \\ 0 \\ 0 \end{pmatrix} \rightarrow \begin{pmatrix} \alpha \\ \delta \\ \epsilon \end{pmatrix} = \begin{pmatrix} -\frac{2c}{c+s} & -\frac{2c}{c+s} \\ -\frac{1}{c+s} & -\frac{c+s+1}{c+s} \\ \frac{c-s+1}{c+s} & \frac{2c+1}{c+s} \end{pmatrix} \begin{pmatrix} \beta \\ \gamma \end{pmatrix}, \tag{2.7}$$

where $c := \cos(\chi)$ and $s := \sin(\chi)$. The vertices become

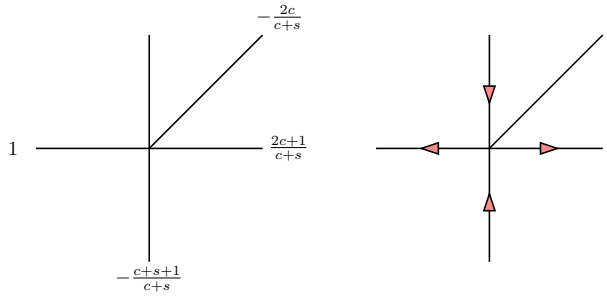

Figure 2.12: Modified vertices.

The left vertex increments that underlie the linear decay mechanism now depend on χ. This gives us a modified recursive rule,

$$\chi_{n+1} = \chi_n + (1 + \frac{1}{\sqrt{2}\sin(\frac{\pi}{4} + \chi_n)}) \prod_{k=0}^{n-1} \tan(\frac{\pi}{4} - \chi_k)\Delta_0, \tag{2.8}$$

where χ_i and $\chi_i + \Delta_i$ are the two χ parameters that alternate in the i-th layer. As shown in Fig.2.13, this creates an effective penetration depth of about $\frac{1}{2\Delta_0}$ for the linear decay mechanism, after which the mode simply becomes the usual counter-rotating squares mechanism. One might also note that the hourglass parameter remains safely small throughout the process. The nonlinear recurrence of Eq.2.8 comprises fixed points at $\chi = -\frac{\pi}{2}$ and $\chi = \frac{\pi}{4}$. The former corresponds to a fully folded mechanism, while

the latter corresponds to our pentagon degenerating in a trapezoidal shape. $\Delta_0 = 0$ is another fixed point and corresponds ot the counter-rotating squares mechanism.

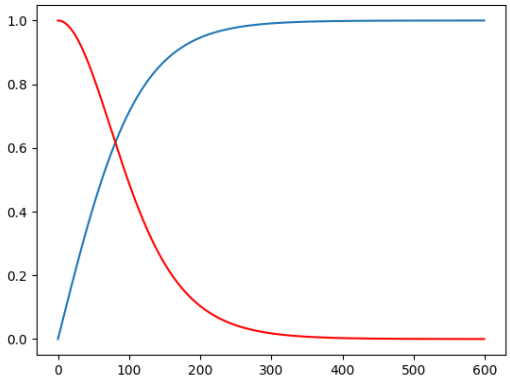

Figure 2.13: Numerical evaluation of the recursion relation of Eq.2.8 with $\chi_0 = 0$ and $\Delta_0 = 0.00001$. The blue curve represents the normalized χ parameter, and the red curve represents the normalized hourglass parameter.

Chapter 3

Tiling Zoology

3.1 Periodic configurations

In this section, we will restrict our attention to periodic configurations, which must respect the crystallographic restriction theorem as well as the Lieb lattice symmetries. The allowed rosette groups are then three cyclic groups (C_1, C_2 and C_4) and three dihedral groups (D_1, D_2 and D_4). *A priori*, this restricts the allowed wallpaper groups to $p1$, $p2$, pm, pg, cm, pmm, pmg, pgg, cmm, $p4$, $p4m$ and $p4g$. In order to see whether tiling symmetries have any bearing on the mode number, shape and localization, we will specify the wallpaper group of each tiling described in the following subsections. We will also highlight the fundamental mechanisms presented in the previous chapter whenever they are present. The counter-rotating squares mechanism will however not be indicated, since its presence is guaranteed for all tilings. We obtain another lower bound on the number of mechanisms by combining an explicit identification of localized states of self-stress and the index theorem. We will use n for the number of cells on the left-right axis, and m for the number of cells on the top-down axis. Up to the presence of surface modes of depth 1, there are 10 different tilings with 2×2 primitive cells. The vertex graphs of the other 246 tilings are congruent to these 10, if we erase open-ended diagonal edges.

3.1.1 (p1)

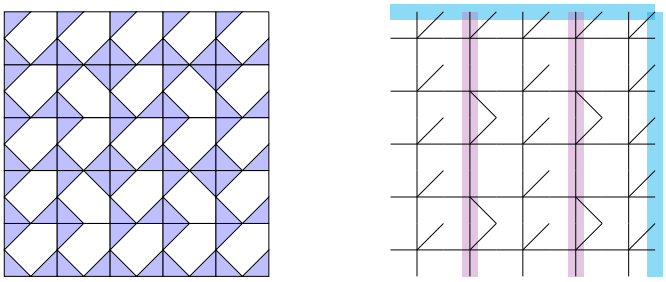

Figure 3.1:

This tiling exhibits $p1$ symmetry. It admits bump modes along one direction but not the other. In addition, it may exhibit up to two surface shears, depending on whether the associated dimension is odd or even-numbered. Explicit listing for n even yields $n/2 + 1$ mechanisms.

3.1.2 Bump modes (p2)

This tiling exhibits $p2$ symmetry. It admits bump modes along one direction but not the other. In addition, it possesses two linear decay sublattices, thus allowing for the four associated linear decay

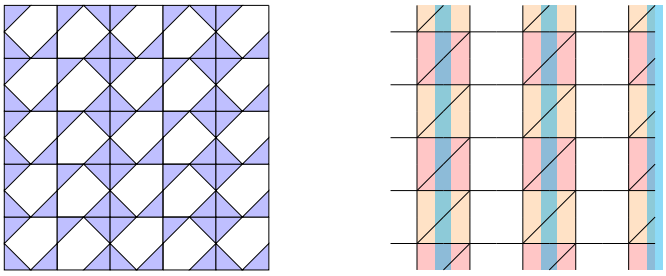

Figure 3.2: A tiling that admits a number of modes scaling with the perimeter.

modes. Explicit listing for n even yields $n/2 + 4$ mechanisms. As shown in Fig.4.2, this overcounts the modes by two. We can guess that the four linear decay mechanisms are actually two, because they have the same orientation.

3.1.3 (pm)

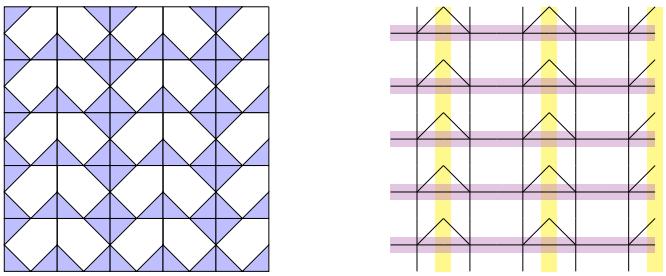

Figure 3.3: pm

This tiling exhibits *pm* symmetry. It admits bump modes along one direction but not the other. In addition, it may exhibit up to one surface shear, depending on whether n is odd or even. Explicit listing for n even yields $n/2 + m + 1$ mechanisms. As shown in Fig.4.3, this overcounts the modes by one. Can we explain that?

3.1.4 (cm:1)

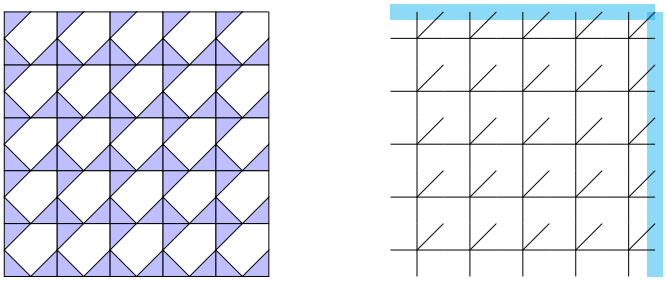

Figure 3.4:

This tiling exhibits *cm* symmetry. It only admits counter-rotations and two surface shears, totalling three mechanisms. A variant of this tiling with only one mechanism will be described in subsection 3.1.9, reflecting a general design principle for surface shear modes.

3.1.5 (cm:2)

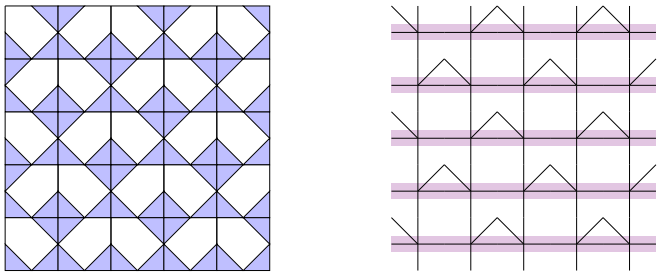

Figure 3.5: Another cm

This tiling also exhibits *cm* symmetry, albeit with a greater period. It admits domain-wall modes along one direction but not the other. Explicit listing for n and m even yields $m + 1$ mechanisms.

3.1.6 (cm:3)

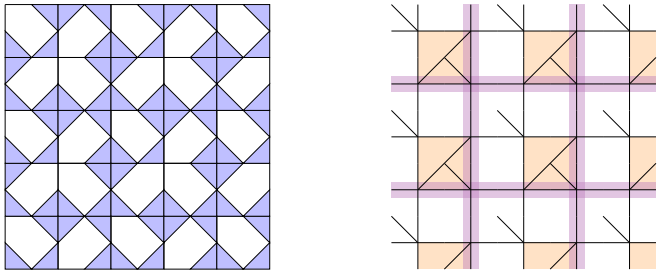

Figure 3.6: Another cm

Yet another tiling with *cm* symmetry. It admits domain-wall modes along both directions. It also allows for a linear decay mechanism. Explicit listing yields $n/2 + m/2 + 2$ mechanisms. As shown in Fig.4.6, this overcounts the modes by one. This might be because we can express linear decays through domain wall mechanisms, if the two directions are available?

3.1.7 (cm:4)

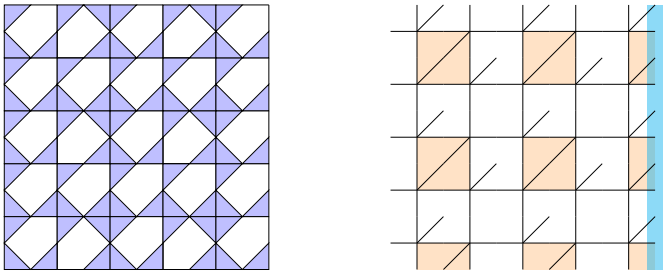

Figure 3.7: Another cm

Our final tiling with *cm* symmetry admits a linear decay sublattice and up to one surface shear, depending on whether n is odd or even. Explicit listing yields 2 mechanisms.

3.1.8 (p4m)

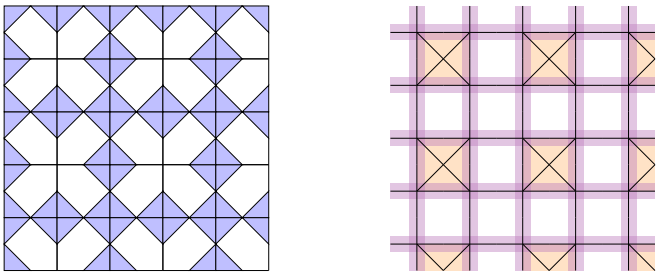

Figure 3.8: p4m

This tiling exhibits *p4m* symmetry. It admits domain-wall modes along both directions. In addition, it allows for a linear decay mechanism. Explicit listing yields $n+m+2$ mechanisms. As shown in Fig.4.8, this overcounts the modes by two, probably for the same reason as $cm:3$.

3.1.9 Counter-rotations (pmg)

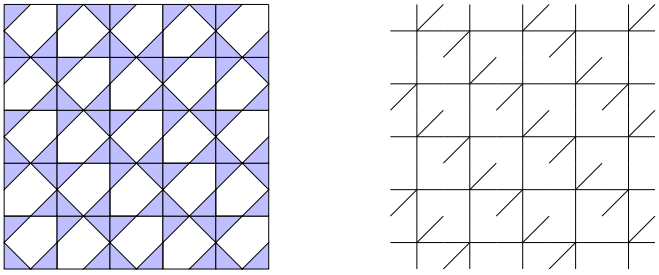

Figure 3.9: A tiling that only admits the counter-rotating squares mechaism.

This tiling exhibits *pmg* symmetry. It is unimodal, only admitting counter-rotations.

3.1.10 (pmg:2)

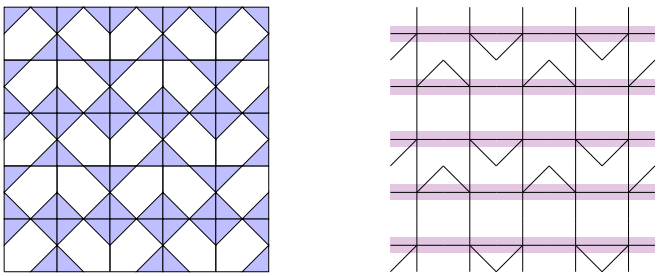

Figure 3.10: Another pmg

This tiling also exhibits *pmg* symmetry. It admits domain-wall modes along one direction but not the other. It seems essentially equivalent to the tiling depicted in Fig.3.5. Explicit listing yields $m+1$ mechanisms.

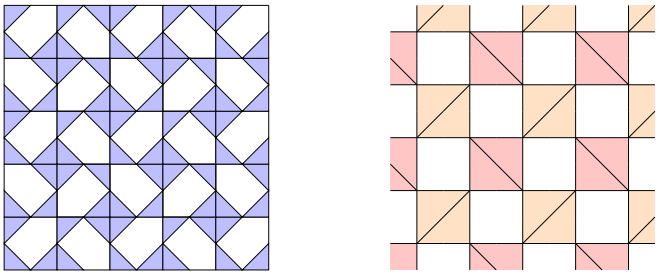

Figure 3.11: A tiling that admits four floppy modes.

3.1.11 Linear decay modes (p4g)

This tiling exhibits *p4g* symmetry. It admits two linear decay sublattices. Explicit listing yields 4 mechanisms. The combinatorial problem in this specific case might have a solution in the litterature, in relation with the orthogonal dimer lattice. Dig deeper.

3.1.12 Bigger primitive cells

We discuss the case of bigger primitve cell using an iterative procedure to see whether new types of modes arise. We also discuss realisations of the missing wallpaper groups: *pg*, *pmm*, *pgg*, *cmm* and *p*4.

3.2 Aperiodic configurations

A further class of arrangements can be investigated, that of non-crystalline configurations.

3.2.1 Random configurations

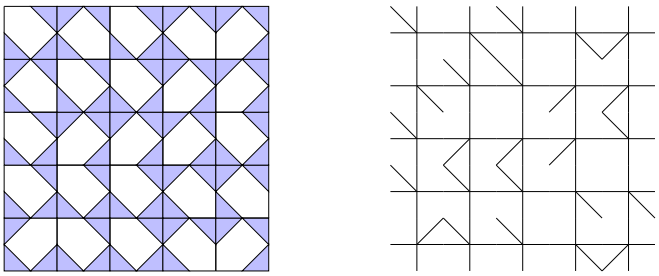

Figure 3.12: A random tiling.

We first consider the generic random case, to understand the generic properties of configurations. As Fig.**??** shows, random configurations typically admit only counter-rotations.

3.2.2 Ordered aperiodic configurations

Can we realize some rosette groups that are forbidden by the crystallographic restriction theorem through aperiodic tilings? These configurations might admit non-trivial modes.

Chapter 4

Numerical and experimental validation

4.1 Compatibility matrix

We conduct a sanity check by computing the size of the compatibility matrix kernel on 11 tesselations for various sizes, in order to confirm the above analysis.

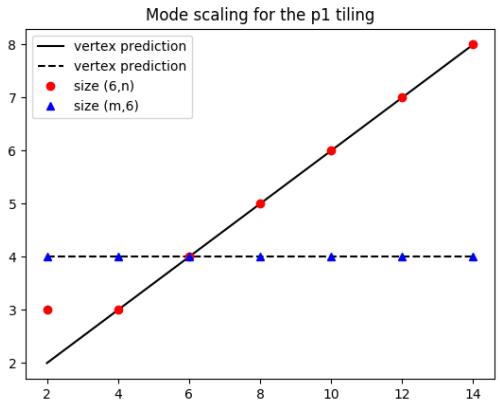

Figure 4.1: Size dependency of the number of zero modes for the $p1$ tiling.

4.2 Finite element simulations

What are the nonzero modes? Does the degeneracy of the zero modes survive real hinges?

4.3 Elasticity experiments

Are there interesting experiments or applications? Do they confirm vertex+FEM? Waveguide? Decay competition?

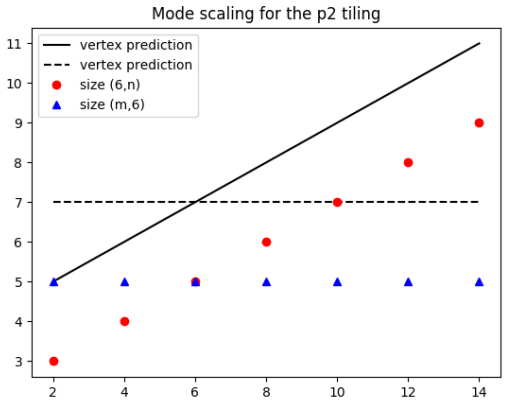

Figure 4.2: Size dependency of the number of zero modes for the $p2$ tiling.

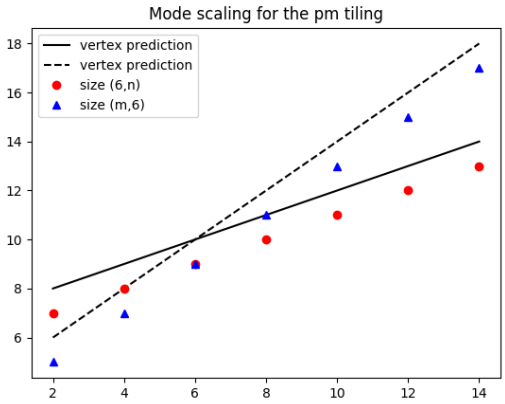

Figure 4.3: Size dependency of the number of zero modes for the pm tiling.

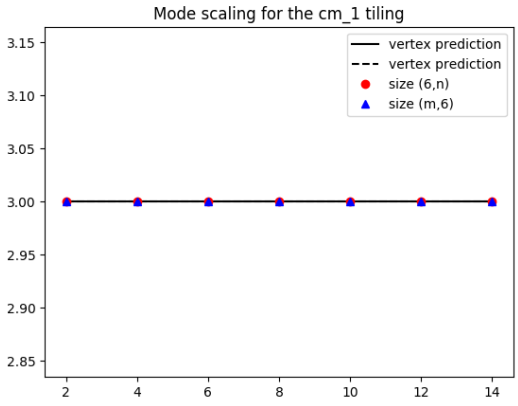

Figure 4.4: Size dependency of the number of zero modes for the first cm tiling.

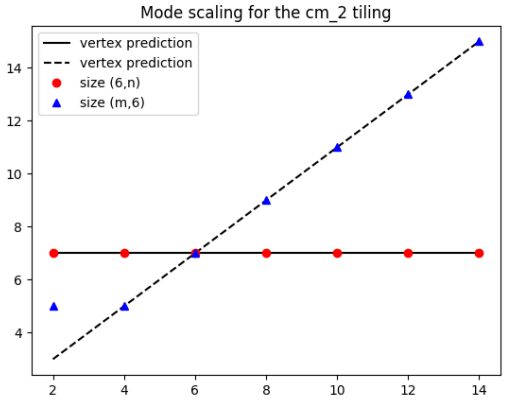

Figure 4.5: Size dependency of the number of zero modes for the second *cm* tiling.

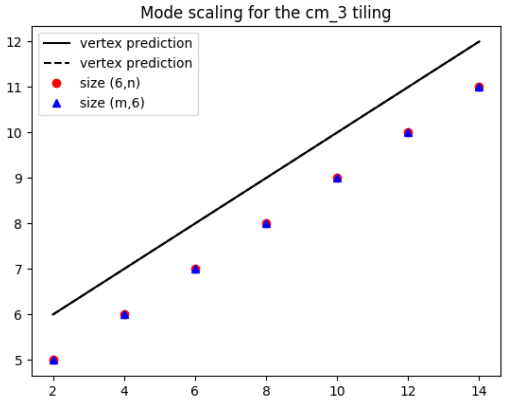

Figure 4.6: Size dependency of the number of zero modes for the third *cm* tiling.

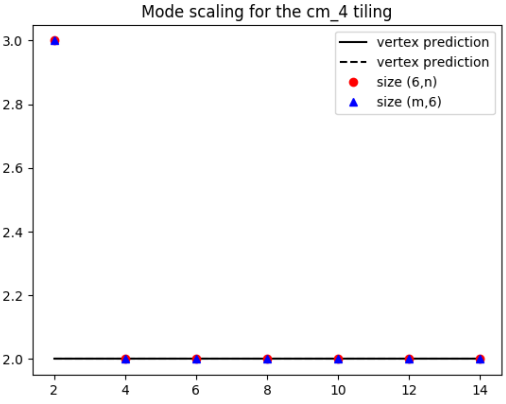

Figure 4.7: Size dependency of the number of zero modes for the fourth *cm* tiling.

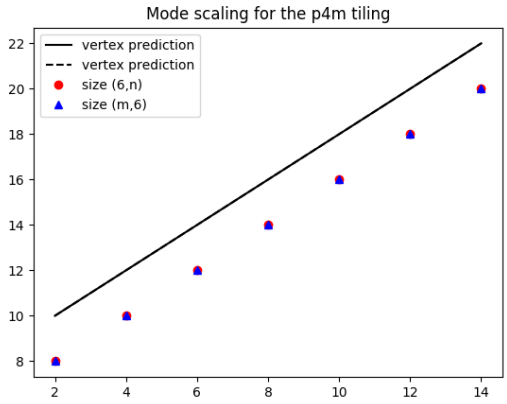

Figure 4.8: Size dependency of the number of zero modes for the $p4m$ tiling.

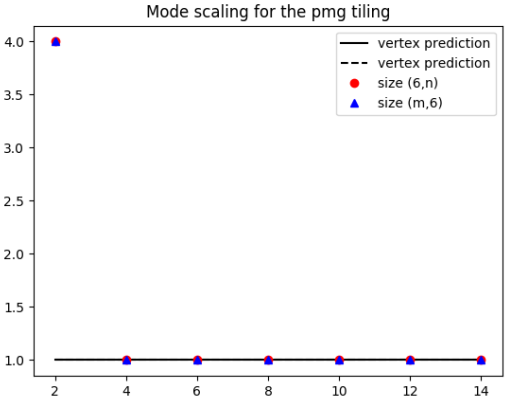

Figure 4.9: Size dependency of the number of zero modes for the pmg tiling.

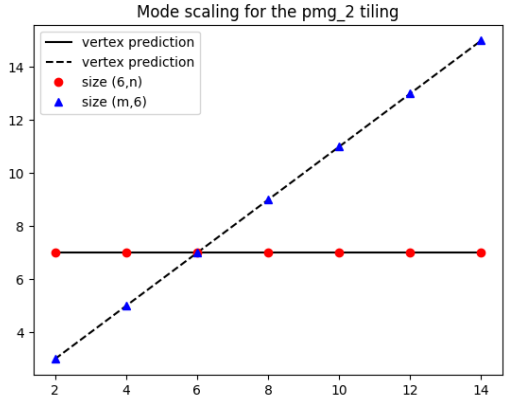

Figure 4.10: Size dependency of the number of zero modes for the second pmg tiling.

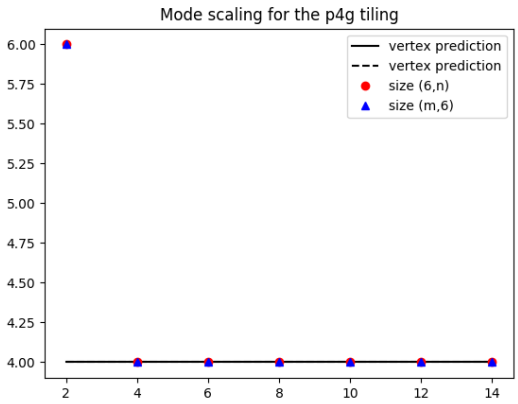

Figure 4.11: Size dependency of the number of zero modes for the $p4g$ tiling.

Chapter 5

Concluding remarks

A 3D version of the primitive cell used throughout this work can be created by "emptying" one or several corners of Corentin's unimodal combinatorial cell. Is it necessary to complement the tile set to obain a solvable combinatorial problem?

Acknowledgements

I would like to thank Corentin for numerous and useful discussions about this project, as well as Tristan of the mechanical workshop for putting up with me as I was learning how to use a laser cutter without burning the building to the ground.

Bibliography

[1] T. C. Lubensky, C. L. Kane, Xiaoming Mao, A. Souslov and Kai Sun. Phonons and elasticity in critically coordinated lattices. *Rep. Prog. Phys.*, 78, 2015.

[2] R. B. Kershner. The Law of Sines and Law of Cosines for Polygons. *Mathematics Magazine*, 44:150–153, 1971.

Appendices

Appendix A

Linearized geometric constraints for triangular lattices

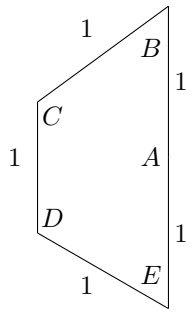

Figure A.1: The equilateral pentagon in the reference position.

The geometric constraints put forward by the side lengths of the pentagon can be expressed as

$$A + B + C + D + E = 3\pi, \tag{A.1}$$

$$2 - 2\cos(A) = 3 - 2\cos(C) - 2\cos(D) + 2\cos(C + D), \tag{A.2}$$

$$\sin(D) - \sin(D + E) = \sin(C) - \sin(C + B). \tag{A.3}$$

We can linearize these expressions around the

$$A = \pi + \alpha \quad B = \frac{\pi}{3} + \beta \quad C = \frac{2\pi}{3} + \gamma \quad D = \frac{2\pi}{3} + \delta \quad E = \frac{\pi}{3} + \epsilon \tag{A.4}$$

choice of angles, yielding the following system of linear equations,

$$\begin{pmatrix} 1 & 1 & 1 & 1 & 1 \\ & 1 & & & 1 \\ & 1 & 2 & -2 & -1 \end{pmatrix} \begin{pmatrix} \alpha \\ \delta \\ \epsilon \\ \beta \\ \gamma \end{pmatrix} = \begin{pmatrix} 0 \\ 0 \\ 0 \end{pmatrix} \rightarrow \begin{pmatrix} \alpha \\ \delta \\ \epsilon \end{pmatrix} = \begin{pmatrix} -2 & -1 \\ & -1 \\ 1 & 1 \end{pmatrix} \begin{pmatrix} \beta \\ \gamma \end{pmatrix}. \tag{A.5}$$

As expected from the index theorem, there are two free parameters. We express this constraint graphically in Fig.2.2, by drawing the two modes of our pentagon in a convenient basis. Any linear combination of those two vertices is thus also an acceptable vertex.

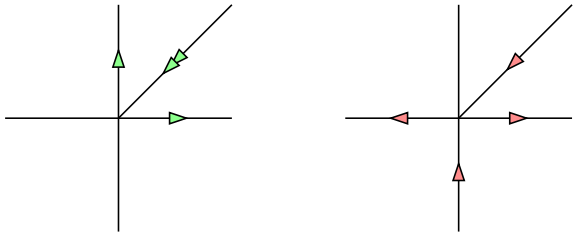

Figure A.2: Graphical representation of the linearized geometric constraints.

Appendix B

Linearized geometric constraints for the inverted prismatic pentagon

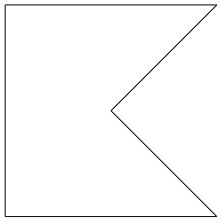

Figure B.1: The inverted prismatic pentagon in the reference position.

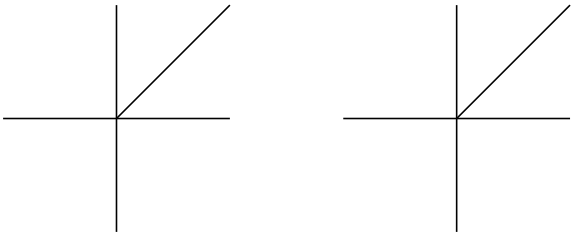

Figure B.2: Graphical representation of the linearized geometric constraints.

Appendix C

Basic states of self-stress

We will now identify a few localized states of self-stress that can occur within our tesselations, in order to obtain an lower bound on the number of mechanisms for a given tiling.

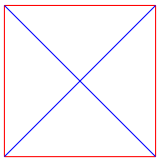

Figure C.1: The textbook example of a state of self-stress.

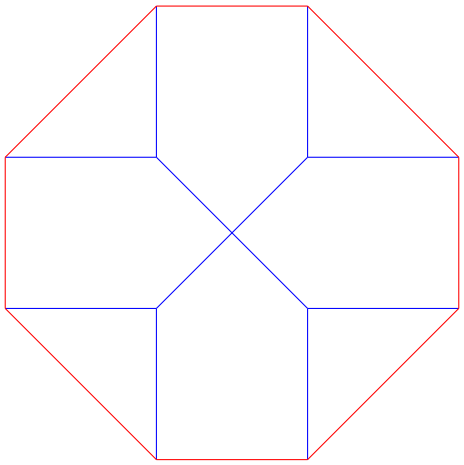

Figure C.2: A less trivial state of self-stress.

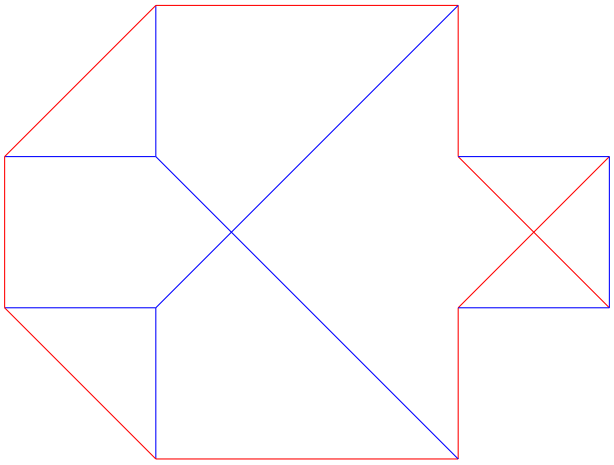

Figure C.3: Another one.